Longitudinal and transverse hyperpolarizabilities of carbon nanotubes: a computational investigation through the coupled-perturbed Hartree–Fock/Kohn–Sham scheme

Valentina Lacivita, Michel Rérat, Roberto Orlando, Roberto Dovesi, Philippe D'arco

Longitudinal and transverse hyperpolarizabilities of Carbon nanotubes. A computational investigation through the Coupled Perturbed Hartree-Fock/Kohn-Sham scheme.

Valentina Lacivita · Michel Rérat · Roberto Orlando · Roberto Dovesi · Philippe D'Arco

Abstract Static electronic polarizability α and second hyperpolarizability γ of semiconduting and conducting carbon nanotubes with radius up to 7.5 Å are evaluated using the coupled-perturbed Hartree-Fock/Kohn-Sham scheme, as implemented in the periodic CRYSTAL14 code, and a split-valence basis set. Two density functionals, namely LDA (pure local) and B3LYP (hybrid), and the Hartree-Fock hamiltonian are compared. A few PBE (gradient corrected) density functional data are also produced for comparison with previous calculations. Convergence of both longitudinal (L) and transverse (T) components is documented. It is shown how the second hyperpolarizability depends critically on the computational conditions, the more so the larger the radius of the nanotube (and thus the smaller the energy gap). The longitudinal component is sensibly affected by the truncation of the exact exchange series (HF and B3LYP), which must include electron-electron interactions at a distance up to 100 Å in order to have γ_L converged to better than 1%. The transverse γ_T component of conducting tubes critically depends on the number of **k** points in reciprocal space: at least 900 **k** points are required to converge better than 1% at the LDA level. Coupled-perturbed results are compared to uncoupled values obtained from a sum-over-states (SOS) approach. The difference between the two is particularly important along the transverse direction and when pure DFT functionals are used: the coupled-perturbed correction can shrink the SOS value by several hundreds times. The ratio LDA/HF is roughly constant around 2 for α_L; it ranges between 25 and 60 for γ_L. As regards the convergence with the nanotube radius, the R^2 law is confirmed for α_L and α_T (normalized for the cell parameter) at all levels of theory. For the second hyperpolarizabilities γ_L and γ_T, a clear R^5 dependence is observed.

V. Lacivita
Institut Calcul et Simulation and Institut des Sciences de la Terre Paris, UPMC, Sorbonne Universités, F-75005 Paris (France)
E-mail: valentina.lacivita@upmc.fr

M. Rérat
Equipe de Chimie Physique, IPREM UMR5254, Université de Pau, 64000 Pau, France

R. Orlando
Dipartimento di Chimica IFM, Università di Torino and NIS - Nanostructured Interfaces and Surfaces - Centre of Excellence, Via P. Giuria 7, 10125 Torino, Italy

R. Dovesi
Dipartimento di Chimica IFM, Università di Torino and NIS - Nanostructured Interfaces and Surfaces - Centre of Excellence, Via P. Giuria 7, 10125 Torino, Italy

Ph. D'Arco
Institut des Sciences de la Terre Paris (UMR 7193 UPMC-CNRS), UPMC, Sorbonne Universités, F-75005 Paris (France)

1 Introduction

All carbon nanotubes (CNTs) are electrically conductive. However, their electronic structure varies depending on the chiral vector (m, n) $(m, n \in \mathbb{N})$: as regards the two important families of armchair (m, m) and zigzag $(m, 0)$ CNTs, the former are $1D$ conductors; the latter are semiconductors with almost vanishing band gap for $m = 3l$ ($l \in \mathbb{N}$). These features, combined with quantum confinement at the nanoscale, originate outstanding optical properties.

Over the past two decades, several theoretical investigations were carried out concerning the linear dielectric response of CNTs [1–6], including a previous work by some of the present authors [7], based on state-of-the-art coupled-perturbed (CP) Hartree-Fock (HF) and Kohn-Sham (KS) *ab initio* calculations with large Gaussian basis sets. Results obtained on a number of zig-zag and armchair single-wall CNTs with radius R up to 16.3 Å, showed the transverse polarizability α_T^a (normalized for the cell parameter a) to scale linearly with the square of the tube radius R, while the longitudinal polarizability α_L^a scales linearly with R/E_g, where E_g is the energy gap.

In recent years, investigations have been extended also to the optical nonlinearity of CNTs [8]. The literature on this topic is abundant on both the experimental and theoretical sides [9–13], but still remains incomplete on many aspects. The properties of interest are the first and second hyperpolarizabilities, β and γ. These are microscopic tensor properties related to the macroscopic dielectric susceptibilities of second ($\chi^{(2)}$) and third order ($\chi^{(3)}$), respectively, through the cell volume V (for a 3D system): $\chi^{(2)} = \frac{2\pi}{V}\beta$ and $\chi^{(3)} = \frac{2\pi}{3V}\gamma$.

The inversion center annihilates the first hyperpolarizability β of armchair and zig-zag nanotubes, not that of general (m, n) tubes. The space symmetry, given by the product of the D_n point symmetry and the axial group of monodimensional translations [14], produces two nonzero β components, namely $\beta_{xyz} = -\beta_{yzx}$. At the static limit, however, the additional tensor permutation symmetry [15], implies $\beta_{xyz}(0; 0, 0)$ to be null. Guo *et al.* [3] calculated "unscreened" (i.e., sum-over-states, SOS) static and dynamic electronic contributions for small chiral nanotubes ($R < 6$ Å), using the local-density approximation (LDA) [16] to the density functional theory (DFT). They found the static value of $\chi_{xyz}^{(2)}(0; 0, 0)$ to be zero indeed, and an absolute value of the second harmonic generation (SHG) coefficient $\chi_{xyz}^{(2)}(-2\omega; \omega, \omega)$ as large as 15×10^{-6} esu in the photon energy range 0.1-4.0 eV. They also noted that the SHG coefficient $\chi_{xyz}^{(2)}(-2\omega; \omega, \omega)$ becomes smaller with increasing R as a consequence of the convergence to graphene, that is center-symmetric.

Second-order optical nonlinearity effects were evaluated by Margulis *et al.* [17] for semiconductor single-wall CNTs. By using a simple two-band approximation, the authors obtained an expression for the static electronic contribution to $\chi^{(3)}$ along the tube axis, that is proportional to the fourth power of the radius R, i.e., $\chi_L^{(3)}(0; 0, 0, 0) \propto R^4$. For a single-wall CNT with radius around 5.5 Å, they estimated $\chi_L^{(3)}(0; 0, 0, 0)$ to be about 3×10^{-9} esu, which is comparable with the largest third-order dielectric susceptibility $\chi^{(3)}$ observed for III-V

semiconductor compounds. An independent estimate of the static second hyperpolarizability γ_L of semiconductor CNTs was later provided by Kozinsky and Marzari [5], by applying the numerical finite-field method at the PBE [18] DFT level. For a zig-zag nanotube $(8, 0)$ of 3.15 Å radius, they obtained $\gamma_L = 3.1 \times 10^7$ a.u. That is, $\chi_L^{(3)} \approx 1 \times 10^{-9}$ esu, if we define an approximate volume $V = \pi R^2 a$, with $a \approx 4$ Å the cell parameter. Although this result is not directly comparable with that obtained by Margulis *et al.*, based on the proposed R^4 law, the ratio between the given radii, i.e., 5.5 Å [17] and 3.15 Å [5], would lead to guess a difference of about one order of magnitude between the corresponding values of $\chi_L^{(3)}$, which is not the case for the data provided by the authors. Further analysis is required in order broaden the spectrum of available absolute data and thus establish reliable trends.

In this paper, we aim to complement and improve upon the above mentioned theoretical results. As a development of our previous study [7], we report about *ab initio* static electronic hyperpolarizability calculations on CNTs of increasing radius, performed using the coupled-perturbed Hartree-Fock/Kohn-Sham (CPHF/ KS) computational scheme, as implemented in the quantum chemistry software package for periodic systems CRYSTAL14 [19–24]. A development version of this code is now under test, which also implements the CP calculation of dynamic SHG coefficients. These features will be investigated in a forthcoming paper.

Unlike SOS perturbative methods, as those applied in Refs. [3] and [17], the coupled-perturbed approach fulfills a self-consistent computational procedure to account for orbital relaxation effects induced by the electric field, thus providing far more accurate optical properties. Furthermore, the analytical character of the CP equations largely overcomes, for both accuracy and efficiency, the variational finite-field approach used in Ref. [5]. We will compare HF and various density functionals, namely conventional local density (LDA) and generalized gradient (PBE) approximations, and the hybrid B3LYP functional. Periodic CPKS calculations represent a severe test of the methodology. It is known that DFT methods may significantly overshoot the electronic (hyper)polarizabilities of extended π-conjugated systems. An example is that of polyenes [25,26], for which only slight (or even no) convergence towards the periodic limit is found [27]. However, we will show that there is no such overshoot in the case of CNTs, as indicated by a fairly good agreement with the experimental data.

We describe here a robust procedure for the evaluation of the optical properties of CNTs, even in cases where the calculated values blow-up as $E_g \to 0$. In do-

ing so, we will show that it is possible to draw regular trends with increasing R at every level of theory, regardless of the convergence rates and of the magnitude of the numbers to be managed.

The paper is organized as follows. Computational details are illustrated in Section 2, with particular focus on the most critical parameters, i.e., the number of **k** points at which the SCF and CP equations are solved and the thresholds controlling the truncation of the exact exchange series. Results are presented in Section 3, dealing with a) the trends of α and γ with increasing radius; b) the comparison between the various levels of theory. Finally, in the last section, a few conclusions are drawn.

2 Computational details

Calculations were performed with the periodic *ab initio* CRYSTAL14 code [19] by using an all-electron split-valence 6-31G(d) basis set. Two density functionals, LDA [28], and B3LYP [29] (containing 20% of exact exchange) are compared with Hartree-Fock (HF). Some calculations have been performed also with the PBE functional, which was previously shown to behave similarly to LDA for the kind of properties investigated here [27].

The geometry was optimized in all cases. The threshold for the convergence of the self-consistent-field (SCF) energy was set to 10^{-10} Ha. The density functional exchange-correlation contribution to the total energy was computed using a pruned grid (keyword `XLGRID` [19]) for numerical integration. Its accuracy can be estimated from the error in the electronic charge per unit cell: $4 \times 10^{-4} |e|$ for a total number of 240 $|e|$ for the (10,0) nanotube. To exit the self-consistent CPHF/KS process, the variation of α (γ) calculated at two subsequent cycles must be smaller than 10^{-2} a.u. (1 a.u.).

CPHF/KS results for small (null) band gap systems are strongly affected by the shrinking factor S used for sampling the reciprocal space, and by the truncation of the infinite exact exchange series (HF and B3LYP cases), as previously documented for polyacetylene [27]. Convergence becomes more critical for large R tubes, because the energy gap narrows ($E_g \propto 1/R$) and polarization effects increase. To describe the effect of the aforementioned computational parameters on the calculated optical properties, we will take as references the $(17,0)$ and $(11,11)$ tubes. These are representatives of semiconducting and conducting CNTs, respectively, and have the largest radii here considered. For the $(11,11)$ CNT we will investigate the convergence of α_T and γ_T, the longitudinal components being infinite as the solution is metallic. For the $(17,0)$ CNT, instead,

we will focus on α_L and γ_L which are finite although very large, whereas the transverse components converge much faster.

2.1 Shrinking factor

A dense **k**-point sampling of the Brillouin zone (BZ) is crucial for the accurate description of the electronic structure around the region where the gap is small. This justifies the need for using a large shrinking factor S to achieve convergence on the calculated optical properties. Pure density functionals (e.g., LDA and GGA) are particularly concerned since they are known to systematically underestimate the band gap. At the other extreme HF overestimates E_g. Table 1 shows the dependence on S of the (hyper)polarizabilities α^C and γ^C (normalized to one C atom), calculated at both the LDA and HF levels of theory. For the $(17,0)$ tube, HF provides an energy gap about four times larger than LDA, producing α_L^C and γ_L^C values that are about 2 and 60 times smaller. All HF and LDA properties are converged to better than 1% at $S = 80$ (41 **k** points). A much slower convergence with S is found for the transverse properties of the $(11,11)$ tube, that is metallic. In this case, the LDA/HF ratio reduces to about 1 for α_T^C, and to 2 for γ_T^C. Asymptotic limits (by fitting) for γ_T^C are 8330 a.u. (LDA) and 4856 a.u. (HF). At the LDA level, the threshold of 1% deviation from the asymptotic limit is only reached at $S = 1800$, that is, using 901 **k** points in the BZ. The same target is achieved at the HF level using 751 **k** points ($S = 1500$).

2.2 Truncation of the exchange series

In extended systems with small gap, the range of the density matrix (represented in the direct space) weighing the integrals of the infinite bi-electronic exchange series is widespread. Hence, the slow convergence of the optical properties with the number of terms that are included in the summation [30].

In CRYSTAL, the truncation of the infinite Coulomb and exchange series is established through five thresholds, T_i ($i = 1 \ldots 5$), such that integrals are disregarded (or approximated) when the *overlap* between the involved functions is below 10^{-T_i} (see Ref. [19] for details). Our previous work on polyacetylene [27] showed that T_1, T_2 and T_3 converge rapidly, as the measure of decay of the overlap of two gaussians, so that their value may safely be set to 10. More delicate is the role of T_4 and T_5, which are associated to the exact exchange summations. We set their values according to the scheme $T_4 = \frac{1}{2}T_5 = T_x$. Table 2 reports α^C and γ^C (normalized

to one C) of the CNTs $(17,0)$ and $(11,11)$ as functions of T_x. The spatial extension of the exchange interactions is indicated in terms of the maximum electron-electron distance d_{e-e} for the given T_x value. Comparison between HF and B3LYP trends is shown. As regards the $(17,0)$ tube, the two series converge pretty much in the same way despite the HF energy gap being about 3 times larger than the B3LYP one, which accounts for two orders of magnitude of difference on γ_L^C. An explanation may be that the major fraction of exact exchange in HF compensates the effect of the smaller gap in B3LYP. γ_L^C requires at least $T_x = 1500$, which corresponds to about 14×10^6 elements of the reducible Hamiltonian matrix to be evaluated. γ_T^C of the conductor tube $(11,11)$ is far less sensitive to T_x: convergence to 1% is reached at $T_x = 200$ with B3LYP, and at $T_x = 350$ with HF.

3 Results and discussion

3.1 Structure and energy gap

Optimized LDA, B3LYP and HF structures of the CNTs are presented in Table 3. B3LYP provides the largest cell parameters a and radii R; the difference with respect to the most compact geometries provided by HF is however very small (around 0.7% both on a and R).

Let us consider now the variation of the electronic (hyper)polarizabilities with increasing the radius R of the CNTs. In doing so, we will focus primarily on a comparative analysis between LDA and HF, which delimit the variation of the calculated energy gap E_g as shown in Figure 1.

We note that for CNTs with $R < 3.4$ Å the LDA (and B3LYP) band gap collapses with discontinuity (left panel). For larger radii, however, E_g is found to be proportional to $1/R$ (right panel) via a coefficient that depends on the nanotube chirality. In other words, the band gap opening occurring in graphene when the $2D$ sheet is bent to generate a CNT depends on the rolling-up direction. The rolling-up perturbation is related to the interaction coefficient $\mathcal{G}$ that appears in the approximate expression of $E_g(R)$ provided by a simple π-electron model [31,17],

$$E_g \approx \frac{2\mathcal{G}}{3R} \tag{1}$$

From our fittings we get: $\mathcal{G}_{3l+1,0} = 3.82$ (LDA), 5.78 (B3LYP) and 16.3 (HF) eV Å; $\mathcal{G}_{3l+2,0} = 6.12$ (LDA), 9.68 (B3LYP) and 21.5 (HF) (B3LYP) eV Å. These results show that the order of effectiveness of the rolling-up perturbation is $3l + 2, 0 > 3l + 1, 0$ for the different families of semiconductor CNTs, and that it is HF $\gg$ B3LYP $>$ LDA for the different levels of theory.

3.2 Electronic polarizability

Table 4 lists the longitudinal and transverse polarizability components for the CNTs here investigated.

3.2.1 Longitudinal component

Upon increasing the radius by a factor 2.4, i.e., from 2.8 Å for the CNT $(7,0)$ to about 6.7 Å for the CNT $(17,0)$, the longitudinal polarizability per C atom α_L^C undergoes an overall increment of about 25-29%, with a ratio LDA/HF roughly constant around 2. The coupled-perturbed self-consistent process modify the SOS value (in parentheses) in opposite directions and by different amounts: decreases by 2% for LDA, increases by 100% for HF.

In the left panel of Figure 2, the longitudinal polarizability per unit length, α_L^a, is plotted against R^2. Regular linear trends are shown for both LDA and HF CNTs and the fittings for the different series of semiconductors draw almost parallel lines. Moreover, for CNTs with $R \geq 3.4$ Å we are allowed to replace R^2 by the R/E_g law expected for α_L^a (Figure 2, right panel), given the above mentioned relationship of inverse proportionality between R and E_g.

One may understand such a R/E_g law by referring to the SOS expression for the static diagonal polarizability [32], i.e.,

$$\alpha_{xx} = \sum_{m \neq 0}^{\infty} \frac{x_{0m} x_{m0}}{\omega_{0m}} \tag{2}$$

where $x_{ij} = \langle i|\mu_x|j\rangle$ is the transition moment between the states i and j, and ω_{0j} is the energy of the transition between the ground state 0 and the state j. In case of small band gap systems such as CNTs, the fundamental transition between the top of the valence band and the bottom of the virtual band becomes predominant because $\omega_{01} \equiv E_g \to 0$. Therefore, Eq. 2 can be simplyfied as

$$\alpha_{xx} \approx \frac{x_{01}^2}{E_g} \tag{3}$$

The square of the transition moment at the numerator of Eq. 3, $x_{01}^2 = x_{01} x_{10}$, expresses a probability of the transition that is inherently proportional to the number of atoms involved. Now, regarding CNTs, since the number of C atoms on the circumference depends directly on the radius of the tube, from Eq. 3 we retrieve the relationship $\alpha_L^a \propto R/E_g$.

3.2.2 Transverse component

The difference between the LDA and HF band structures has a negligible effect on the transverse tensor

components. This is in agreement with earlier calculations performed in the linear regime on both semiconducting and metallic tubes [1,33,5]. Indeed, for all nanotubes, CP LDA and HF transverse polarizabilities α_T converge to a ratio of about 1, Figure 3. As regards the SOS values of α_T, instead, an initial LDA/HF ratio of about 2.5 is found, which increases almost linearly with increasing R.

By considering the evolution of the transverse polarizability normalized for the cell parameter, α_T^a, we find linear LDA and HF trends vs. R^2. This is in agreement with previous results obtained at the B3LYP level [7]. In that case, a fitting slope $s_{\mathrm{B3LYP}} = 0.368$ was obtained, which compared well with the ideal value of $3/8$ derived from the classical model proposed by Bendict et al. [1], namely

$$\alpha_T^{CP} = \frac{\alpha_T^{SOS}}{1 + 2\alpha_T^{SOS}/R^2} \qquad (4)$$

where $\alpha_T^{SOS}/\alpha_T^{CP} \approx 4$. At the LDA level of theory, the ratio $\alpha_T^{SOS}/\alpha_T^{CP}$ increases to about 5, yielding an ideal coefficient of $2/5=0.4$ that is still quite close to the fitting result, $s_{\mathrm{LDA}} = 0.47$. In contrast, HF diverges from expectations: the slope provided by the fit is $s_{\mathrm{HF}} = 0.41$, to be compared with the value $1/4$ obtained from Eq. 4 and the observed ratio $\alpha_T^{SOS}/\alpha_T^{CP} \approx 2$.

By fitting the ratio α_L/α_T vs. R we obtain asymptotic values at about 3.5 (SOS) and 18.6 (CP) for LDA; at about 3.1 (SOS) and 13.5 (CP) for B3LYP; at 2.6 (SOS) and 10 (CP) for HF. The CP limits turn out to be much higher than the SOS ones.

At the limit for $R \to \infty$ (i.e., the graphene slab xy) it is expected that $\alpha_L \to \alpha_{xx}^{slab}$ and that $\alpha_T \to (1/2)(\alpha_{xx}^{slab} + \alpha_{zz}^{slab}) \approx \alpha_{xx}^{slab}/2$ (the finite value of α_{zz}^{slab} is negligible with respect to the infinite α_{xx}^{slab} value). Therefore, the ratio α_L/α_T should be equal to 2. However, due to the polarization the transversal field felt by the atoms in the tube is less intense than the external field (the depolarization factor along the transverse direction is 2π). It follows a ratio α_L/α_T larger than 2, particularly at the the CP level of calculation which takes better account of this effect. In HF, however, in addition to the depolarization of the transverse field ($\alpha_T^{SOS}/\alpha_T^{CP} \approx 2$) an important effect comes also from the relaxation of the crystalline orbitals along the nanotube axis, i.e., $\alpha_L^{CP}/\alpha_L^{SOS} \approx 2$.

3.3 Electronic second hyperpolarizability

3.3.1 Longitudinal component

Table 5 reports the longitudinal second hyperpolarizabilities of semiconducting nanotubes calculated at the LDA, B3LYP and HF levels of theory. As expected, the longitudinal component strongly depends on the energy gap (see Table 4): the LDA/HF γ_L^C ratio ranges from 25 to 56.

The orbitals relaxation provides a negligible contribution to the calculated LDA values of γ_L^C, the SOS/CP ratio being almost constant around 1 (see Table 5, SOS values in parentheses). In the HF case, on the contrary, the scale factor SOS/CP ranges from 0.15 to 0.35. B3LYP stands midway as usual, with a ratio SOS/CP constant around 0.6.

Figure 5 shows the trend (on a logarithmic scale) of γ_L^a (normalized for the cell parameter) as a function of the radius for the two series of semiconducting CNTs. $(3l + 1, 0)$ and $(3l + 2, 0)$ CNTs show an almost linear trend for radii $R > 3$ Å ($\log R > 0.47$). By fitting each nanotube series with a linear function we get the slopes:

- $s_{3l+1,0} = 4.54$ and $s_{3l+2,0} = 6.12$ for LDA;
- $s_{3l+1,0} = 4.41$ and $s_{3l+2,0} = 5.76$ for B3LYP;
- $s_{3l+1,0} = 4.12$ and $s_{3l+2,0} = 5.43$ for HF.

The average values are 5.33 (LDA), 5.09 (B3LYP) and 4.78 (HF), respectively, showing that γ_L^a depends on the fifth power of the radius. As for α_L^a, we can try to interpret this result looking at the SOS expression for the diagonal component of the second hyperpolarizability tensor in the static limit [32,34], i.e.,

$$\gamma_{xxxx} = \sum_{m,n,p \neq 0}^{\infty} \frac{x_{0m} \bar{x}_{mn} \bar{x}_{np} x_{p0}}{\omega_{0m} \omega_{0n} \omega_{0p}} - \sum_{m,n \neq 0}^{\infty} \frac{x_{0m} x_{m0} x_{0n} x_{n0}}{\omega_{0m} \omega_{0n} \omega_{0n}} (5)$$

where $\bar{x}_{ij} = \langle i|\mu_x|j \rangle - \delta_{ij} x_{00}$. Again, in the case of CNTs contributions other than the "fundamental" transition $0 \to 1$ may be neglected. Hence,

$$\gamma_{xxxx} \approx \frac{x_{01}^2}{E_g^3} (x_{11} - x_{00})^2 - \frac{x_{01}^4}{E_g^3} \qquad (6)$$

By comparing Eqs. 6 and 3, we may assume

$$\gamma_{xxxx} \approx \frac{\alpha_{xx}}{E_g^2} (x_{11} - x_{00})^2 - \frac{\alpha_{xx}^2}{E_g} \qquad (7)$$

to first order. Given that $\alpha_L^a \propto R/E_g$, and that $E_g \propto 1/R$ for reasonably large CNTs, from Eq. 7 we get

$$\gamma_L^a \approx AR^4(x_{11} - x_{00})^2 - BR^5 \qquad (8)$$

where A and B are general proportionality coefficients. Given the positive sign of the calculated γ_L^a, the largest contibution to the second hyperpolarizability of CNTs must arise from the first term on the rhs of Eq. 8. Moreover, given that the $(x_{11} - x_{00})^2$ factor is a linear combination of transition probabilities, it turns out that $(x_{11} - x_{00})^2 \propto R$, which finally yields $\gamma_L^a \propto R^5$. In order to connect the above expression with the R^4 law proposed for the third-order static dielectric susceptibility of CNTs, γ_L is to be normalized for the number

of C atoms in the unit cell, n_C. This corresponds to dividing Eq. 8 by R (being $n_C \propto R$), which provides $\gamma_L^C \propto R^4$, in agreement with Eq. (28) of Ref. [17].

We may compare our analytical result with the numerical PBE estimate of γ_L obtained by Kozinsky and Marzari [5] for the $(8,0)$ tube. They calculated $\gamma_L = 3.1 \times 10^7$ a.u. over a unit cell volume, which corresponds to $\gamma_L^C = 9.7 \times 10^5$ a.u. per C atom. On our side, we optimized the structure of the CNT $(8,0)$ at the PBE level, and then performed a coupled-perturbed PBE calculation of its longitudinal hyperpolarizability, obtaining $\gamma_L^C = 32 \times 10^6$ a.u., which reveals a second-order optical nonlinearity much larger than what Kozinsky and Marzari [5] estimated. In addition, it should be noticed that the PBE and LDA ($\gamma_L^C = 29 \times 10^6$ a.u.) values are very close (about 8% difference), as expected for small band gap monodimensional systems [27].

Now we come to the comparison with experiments. Liu *et al.* [35] measured the third order dielectric susceptibility $\chi^{(3)}$ of various CNTs solutions. For a solution with 0.08 mg/ml carbon they determined the off-resonant longitudinal response of the nanotubes to be 6.460×10^{-14} esu; whence, an average contribution per C atom of about 5.921×10^{-36} esu. Assuming the radius of the nanotubes in the sample to be around 5-6 Å as typical, we may draw a parallel with our calculations on the semiconducting CNTs $(13,0)$, $(14,0)$, $(16,0)$ and $(17,0)$, Tables 3 and 5. Average values of $\chi_L^{(3)}$ per C atom can be obtained from those of γ_L^C via the relation

$$\chi_L^{(3)} = \left(\frac{2\pi}{V} \gamma_L \right) c_f \tag{9}$$

where $1/V = 5.95 \times 10^{-6}$ Bohr^{-3} is the number of C atoms per unit volume as derived from the carbon mass density of the experimental sample, and $c_f = 5.038 \times 10^{-40}$ esu/a.u. is the units conversion factor [36]. The results are $\chi_L^{(3)} = 9.340 \times 10^{-36}, 2.620 \times 10^{-36}$ and 2.261×10^{-37} esu (per C atom) at the LDA, B3LYP and HF levels of theory, respectively. We conclude therefore that, while HF underestimates the nonlinear optical response of CNTs, both density functionals provide $\chi^{(3)}$ values in good qualitative agreement with the experiment.

3.3.2 Transverse component

Transverse second hyperpolarizabilities are reported in Table 6; the order of magnitude of the calculated values is the same, both with respect to the CNT family and the Hamiltonian. At variance with respect to γ_L, CP results for γ_T differ considerably from the SOS values (shown in parentheses).

As regards LDA, coupled-perturbed relaxation effects correct the initial SOS value by reducing it several hundreds times: the ratio SOS/CP can be as large as 850 for semiconducting CNTs and 670 for metallic CNTs. The same applies to B3LYP, although the ratio SOS/CP on γ_T reduces to about 300 for both conductors and semiconductors. The CP HF correction follows the same trend (reduction of the SOS value), but in this case the ratio is around 30-50.

The transverse component γ_T, at variance with respect to γ_L, show rather small quantitative differences between LDA and HF and the LDA/HF ratio always remain smaller that 2. Figure 6 shows the logarithmic trends of γ_T^a (normalized for the cell parameter) obtained for semiconducting and conducting CNTs as a function of R. All series of CNTs follow a linear trend. In all cases the straight lines are essentially parallel to each other (in particular looking at large R values), the fitting slope being again very close to 5.

Figure 7 shows CP ratios γ_L/γ_T as functions of R. One can clearly see that for all Hamiltonians this ratio tends to a horizontal asymptote, unique for the two series of semiconductor CNTs, $(3l+1,0)$ and $(3l+2,0)$. This confirms that longitudinal and transverse second hyperpolarizabilities vary in the same way with R^5. Although being still far from the infinite radius limit, fittings provide an idea of where the asymptotes are placed at the different levels of theory. That is, between 3×10^5 and 6×10^5 for LDA, between 5×10^4 and 9×10^4 for B3LYP, between 2×10^3 and 4×10^3 for HF. We see that the choice of the Hamiltonian covers a range of uncertainty of more than two orders of magnitude. Finally, it is worth noting the large difference with respect to the asymptotes obtained for SOS results: roughly 700 (LDA), 300 (B3LYP) and 100 (HF), on average. This demonstrates the exacerbation in γ (in comparison with α) of the combined effects of field depolarization and crystalline orbitals relaxation that are involved in the coupled-perturbed process.

4 Conclusions

Coupled-perturbed static electronic hyperpolarizabilities of CNTs have been calculated both at the DFT (LDA, PBE and hybrid B3LYP) and HF levels of theory. This provides a large spectrum of performance in the evaluation of the energy gap and, more generally, in the description of the electronic structure. It is shown that DFT second hyperpolarizabilities yield the best agreement with the experiments, which rules out the problem of the DFT overshoot for the present case. In addition, the different density functionals are found to be equivalent in terms of qualitative accuracy.

Predictably, the divergence of DFT methods against HF is found to be far more pronounced on γ than on α. However, the extent of such divergence depends on whether it relates with SOS estimates (unscreened or uncoupled values) obtained ahead of the self-consistent CP process, or with the final CP values corrected via the relaxation of the crystalline orbitals under the effect of the field. In fact, SOS results are generally much more far apart than converged CP values: the ratio LDA/HF can be as large as 400 for γ_L^{SOS} *vs.* 60 for γ_L^{CP}, and 40 for γ_T^{SOS} *vs.* 1 for γ_T^{CP}. In particular, concerning γ_L^{CP}, we found LDA/HF and B3LYP/HF ratios as large as 56 and 15, respectively.

The amount of the CP correction varies depending on the Hamiltonian and on the direction of the field with respect to the nanotube axis. It is just about 2% (4%) for the longitudinal second hyperpolarizability calculated at the LDA (B3LYP) level but it exceeds 600% at the HF level. DFT transverse second hyperpolarizabilities undergo a much larger variation than HF during the coupled-perturbed process: LDA and B3LYP SOS values are reduced by some hundreds times whereas the HF value is scaled only by a few tens of times.

We considered also the influence of the computational parameters on the coupled-perturbed results. Two factors play a critical role for convergence, the more so the larger the radius of the CNT. These are the number of $\mathbf{k}$ points in reciprocal space and the range of exact exchange terms considered (for HF and B3LYP). The first is relevant in particular for conducting CNTs which require up to 900 $\mathbf{k}$ points to converge to better than 1% on γ_T. The second affects particularly γ_L of semiconducting CNTs, so that the exchange series must include contributions from integrals involving electrons more than a hundred angstroms away from each other.

Finally, we determined the nonlinear optical behavior of CNTs with increasing radius. We uphold the law in R^4 predicted by Margulis *et al.* [17] for the macroscopic dielectric susceptibility $\chi_L^{(3)}$, as corresponding to the microscopic longitudinal second hyperpolarizability γ_L^C normalized to one C atom. This is equivalent to an increase in R^5 of the same component normalized for the cell parameter, i.e., γ_L^a. The same trend in R^5 is found for γ_T^a, with respect to which conductor and semiconductor CNTs are essentially aligned.

These results complement and extend the present knowledge on the linear and nonlinear optical behavior of CNTs. In a future work the investigation will be extended to dynamic optical response properties of CNTs. As regards methodology, we provided a detailed analysis of the impact that the computational setting (Hamiltonian, parameters, theoretical approach) may have on the calculated results. The next step will be assessing the effect of the long-range correction to the DFT.

References

1. Benedict, L. X. and Louie, S. G. and Cohen, M. L., Phys. Rev. B **52**, 8541 (1995)
2. Li, Y. and Rotkin, S. V. and Ravaioli, U., Nano Letters **3**(2), 183 (2003)
3. Guo, G. Y. and Chu, K. C. and Wang, D.-S. and Duan, C.-G., Phys. Rev. B **69**, 205416 (2004)
4. Guo, G. Y. and Chu, K. C. and Wang, D.-S. and Duan, C.-G., Comp. Mater. Sci. **30**, 269 (2004)
5. Kozinsky, B. and Marzari, N., Phys. Rev. Lett. **96**, 166801 (2006)
6. Brothers, E. N. and Izmaylov, A. F. and Scuseria, G. E. and Kudin, K. N., J. Phys. Chem. C **112**(5), 1396 (2008)
7. Demichelis, R. and Noël, Y. and D'Arco, Ph. and Rèrat, M. and Zicovich-Wilson, C. M. and Dovesi, R., J. Phys. Chem. C **115**(18), 8876 (2011)
8. Wang, J. and Chen, Y. and Blau, W. J., J. Mater. Chem. **19**, 7425 (2009)
9. Stanciu, C. and Ehlich, R. and Petrov, V. and Steinkellner, O. and Herrmann, J. and Hertel, I. V. and Slepyan, G. Y. and Khrutchinski, A. A. and Maksimenko, S. A. and Rotermund, F. and Campbell, E. E. B. and Rohmund, F., Appl. Phys. Lett. **81**(21), 4064 (2002)
10. Nemilentsau, A. M. and Slepyan, G.Ya. and Khrutchinskii, A. A. and Maksimenko, S. A., Carbon **44**(11), 2246 (2006)
11. Zhu, Y. and Elim, H. I. and Foo, Y.-L. and Yu, T. and Liu, Y. and Ji, W. and Lee, J.-Y. and Shen, Z. and Wee, A. T.-S. and Thong, J. T.-L., Adv. Mater. **18**(5), 587 (2006)
12. Cho, W. B. and Yim, J. H. and Choi, S. Y. and Lee, S. and Schmidt, A. and Steinmeyer, G. and Griebner, U. and Petrov, V. and Yeom, D.-I. and Kim, K. and Rotermund, F., Adv. Funct. Mater. **20**(12), 1937 (2010)
13. Villanueva, G. E. and Jakubinek, M. B. and Simard, B. and Oton, C. J. and Matres, J. and Shao, L.-Y. and Pérez-Millán, P. and Albert, J., Opt. Lett. **36**(11), 2104 (2011)
14. Damnjanovic, M. and Milosevic, I. and Vukovic, T. and Sredanovic, R., J. Phys. A - Math. Gen. **32**(22), 4097 (1999)
15. Kleinman, D. A., Phys. Rev. **126**, 1977 (1962)
16. Vosko, S. H. and Wilk, L. and Nusair, M., Can. J. Phys. **58**, 1200 (1980)
17. Margulis, V. A. and Sizikova, T. A., Physica B **245**(2), 173 (1998)
18. Perdew, J. P. and Burke, K. and Ernzerhof, M., Phys. Rev. Lett. **77**, 3865 (1996)

19. Dovesi, R. and Saunders, V. R. and Roetti, C. and Orlando, R. and Zicovich-Wilson, C. M. and Pascale, F. and Doll, K. and Harrison, N. M. and Civalleri, B. and Bush, I. J. and D'Arco, Ph. and Llunell, M. and Causà, M. and Noël, Y., *CRYSTAL14 User's Manual*. Università di Torino, Torino (2014)

20. Ferrero, M. and Rérat, M. and Orlando, R. and Dovesi, R., J. Comput. Chem. **29**, 1450 (2008)

21. Ferrero, M. and Rérat, M. and Orlando, R. and Dovesi, R., J. Chem. Phys. **128**, 014110 (2008)

22. Ferrero, M. and Rérat, M. and Kirtman, B. and Dovesi, R., J. Chem. Phys. **129**, 244110 (2008)

23. Ferrero, M. and Rérat, M. and Orlando, R. and Dovesi, R. and Bush, I., J. Phys. Conf. Ser. **117**, 12016 (2008)

24. R. Orlando, V. Lacivita, R. Bast, K. Ruud, J. Chem. Phys. **132**, 244106 (2010)

25. Champagne, B. and Perpéte, E. A. and van Gisbergen, S. J. A. and Baerends, E. J. and Snijders, J. G. and Soubra-Ghaoui, C. and Robins, K. A. and Kirtman, B., J. Chem. Phys. **109**, 10489 (1998)

26. Champagne, B. and Perpéte, E. A. and van Gisbergen, S. J. A. and Baerends, E. J. and Snijders, J. G. and Soubra-Ghaoui, C. and Robins, K. A. and Kirtman, B., J. Chem. Phys. **110**, 11664 (1999)

27. Lacivita, V. and Rérat, M. and Orlando, R. and Ferrero, M. and Dovesi, R., J. Chem. Phys. **136**, 114101 (2012)

28. J. P. Perdew and A. Zunger, Phys. Rev. B **23**, 5048 (1981)

29. A. D. Becke, J. Chem. Phys. **98**, 5648 (1993)

30. Causà, M. and Dovesi, R. and Orlando, R. and Pisani, C. and Saunders, V. R., J. Phys. Chem. **92**, 909 (1988)

31. Yorikawa, H. and Muramatsu, S., Phys. Rev. B **52**, 2723 (1995)

32. Orr, B. J. and Ward, J. F., Mol. Phys. **20**, 513 (1971)

33. Brothers, E. N. and Kudin, K. N. and Scuseria, G. E. and Bauschlicher, C. W., Phys. Rev. B **72**, 033402 (2005)

34. Kuzyk, M. G., Phys. Rev. A **72**, 053819 (2005)

35. X. Liu, J. Si, B. Chang, G. Xu, Q. Yang, Z. Pan, S. Xie, P. Ye, J. Fan, M. Wan, Appl. Phys. Lett. **74**(2), 164 (1999)

36. Cox, J. D. and García de Abajo, J. F., Nature Communications **5**, 5725 (2014)
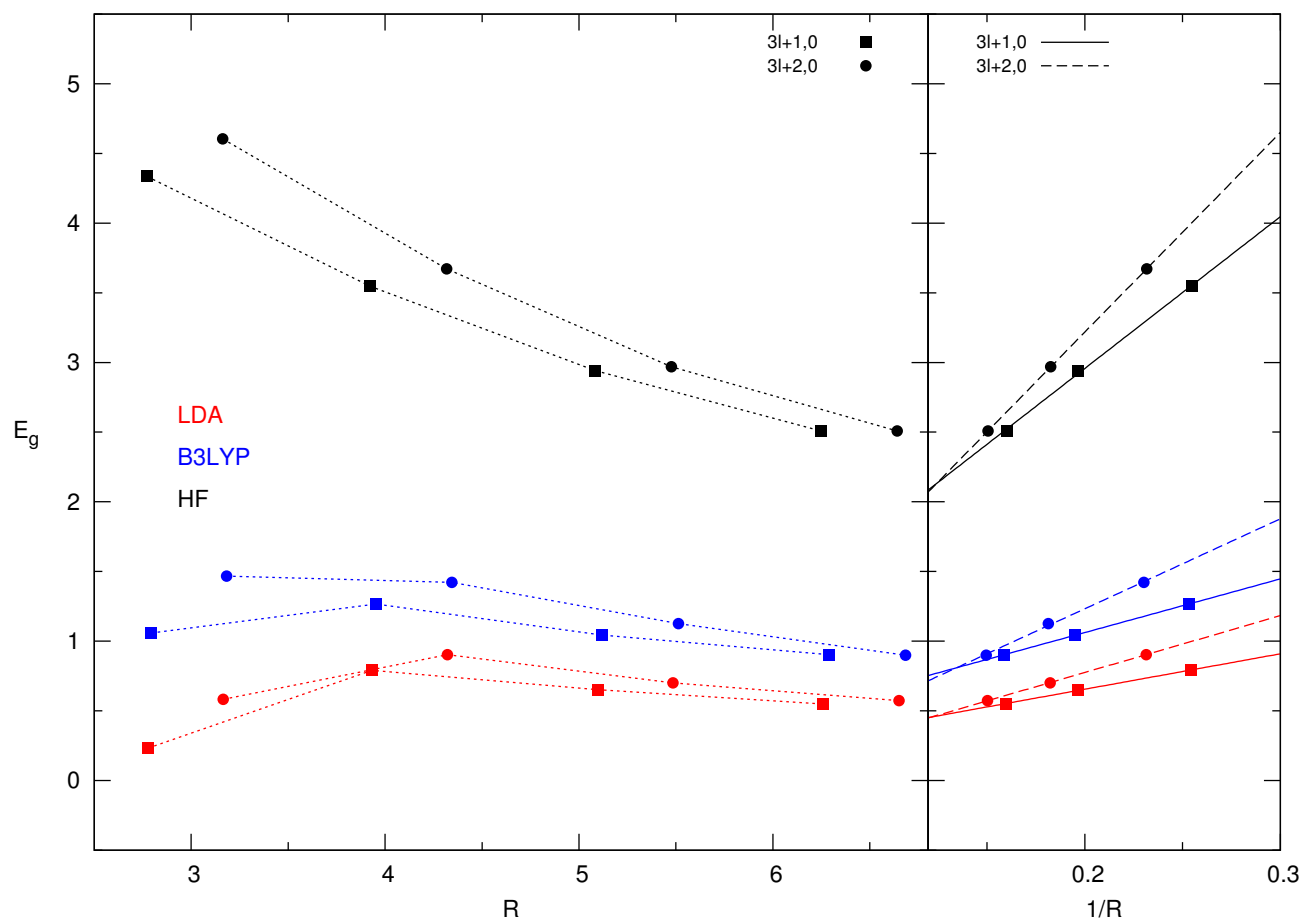
Fig. 1 Energy gap E_g (eV) of semiconductor CNTs as a function of the radius R (Å, on the left), and of the inverse of the radius $1/R$ (Å^{-1}, on the right).
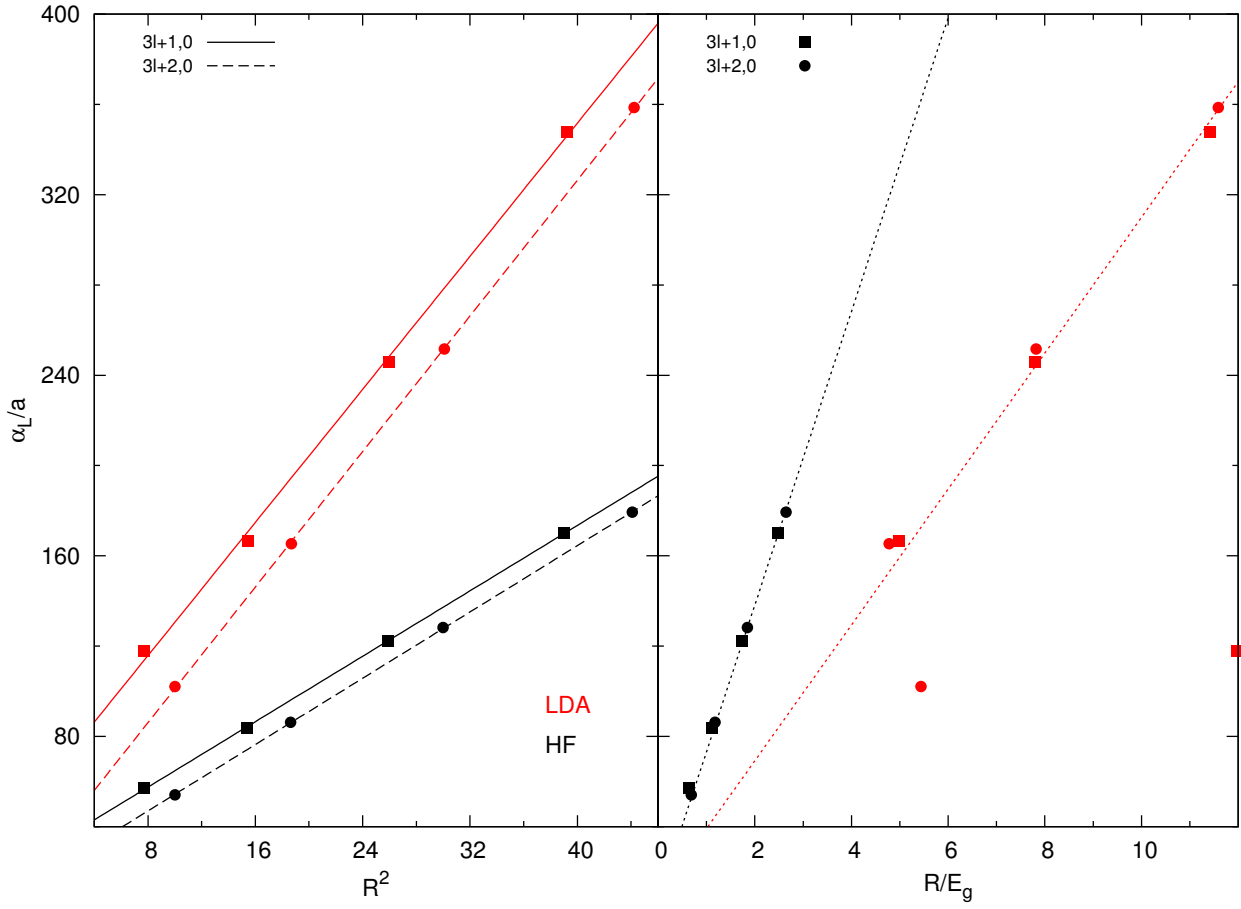
Fig. 2 Longitudinal polarizability per unit length, α_L^a (Å^2), as a function of R^2 (Å^2, left panel), and of R/E_g (Å/eV, right panel). The two LDA points lying outside the straight line (right panel) correspond to the smallest CNTs $(7,0)$ and $(8,0)$ whose band gap is in discontinuity with the trend drawn by the larger CNTs (see text).
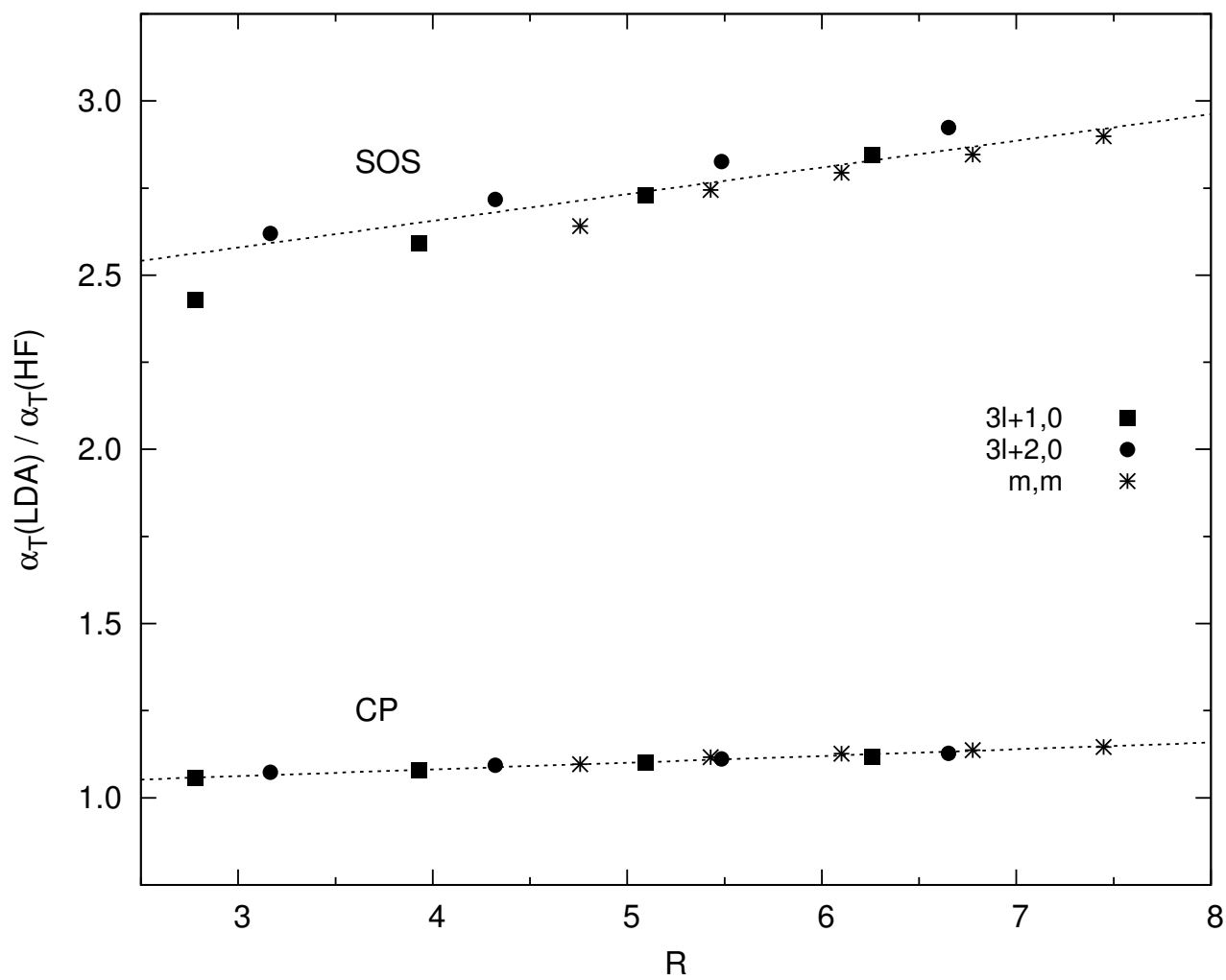
Fig. 3 LDA/HF ratio for α_T as a function of the radius R (Å). Comparison between SOS and CP trends.
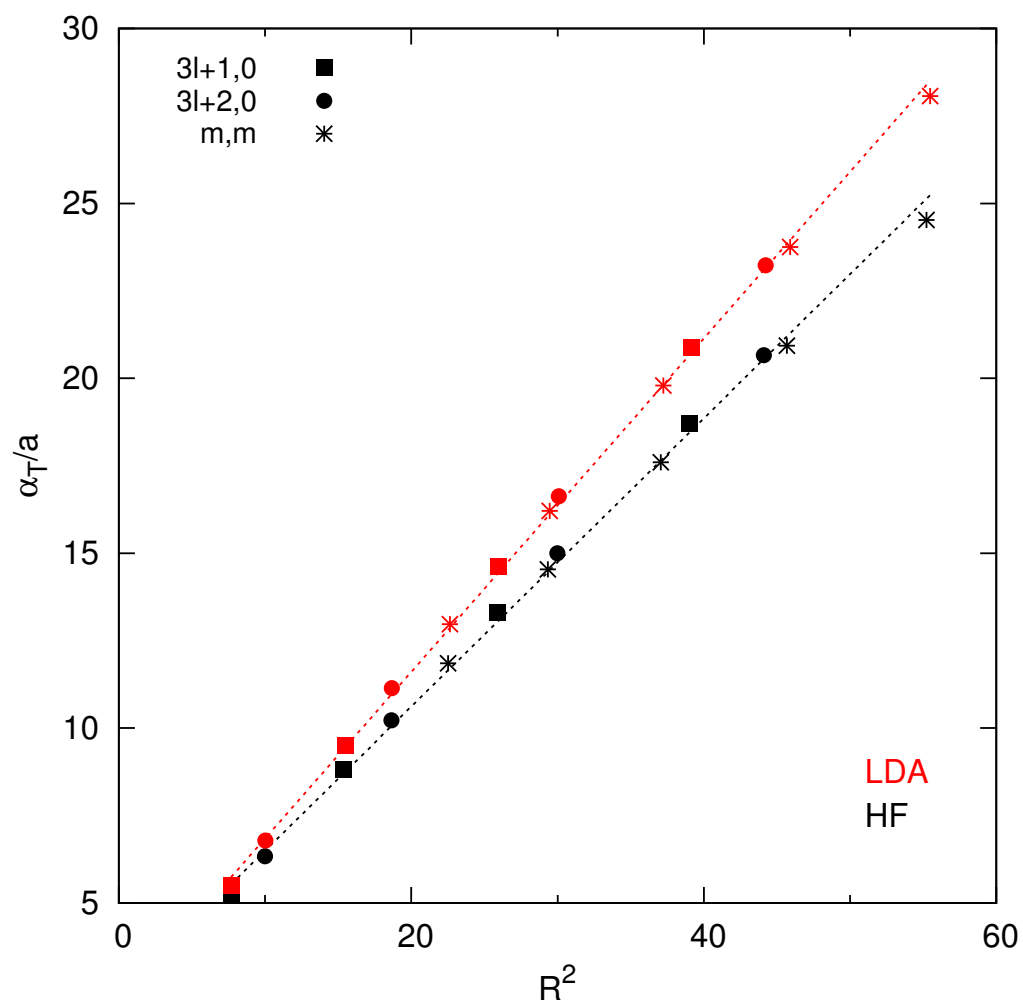
Fig. 4 Transverse polarizability per unit length, α_T^a (Å^2), as a function of the square of the tube radius R^2 (Å^2).
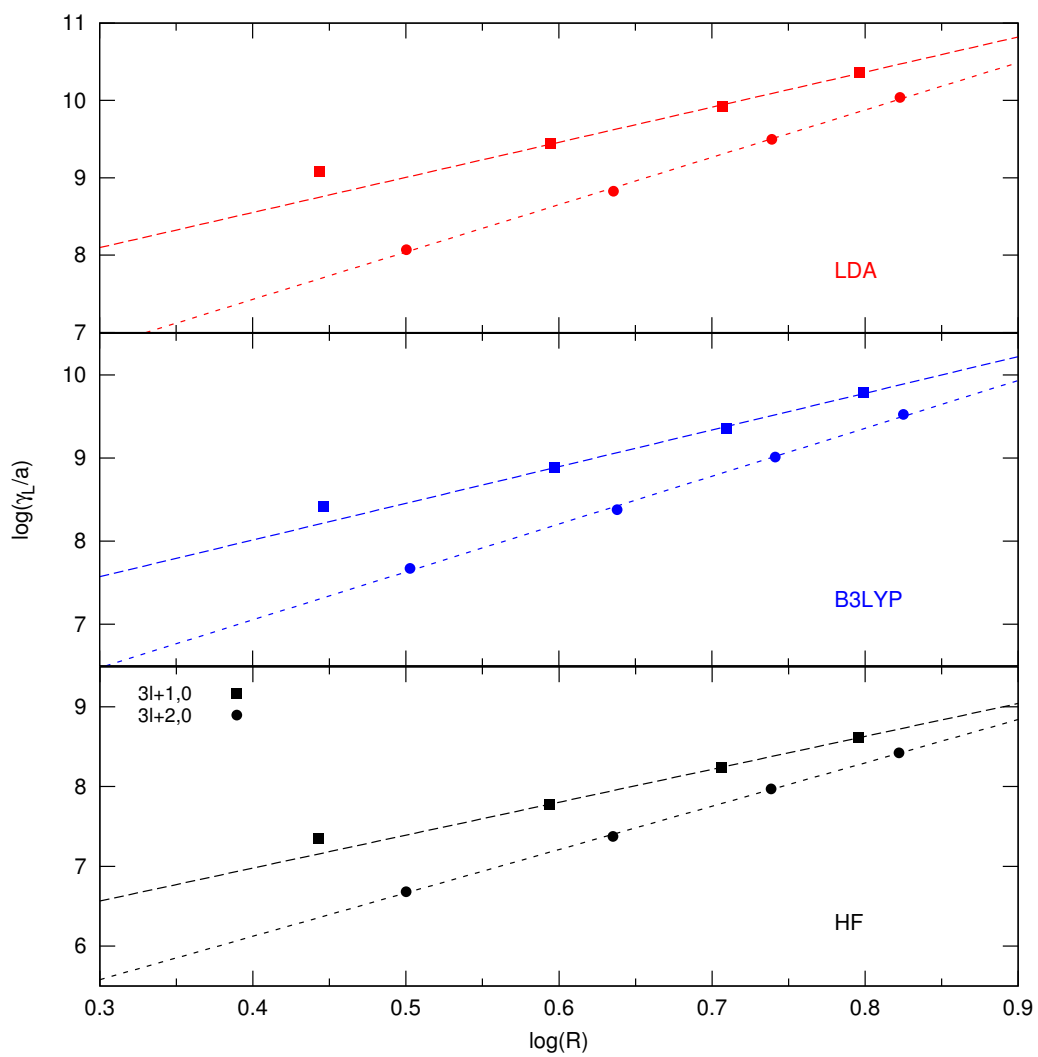
Fig. 5 Logarithmic plot of the longitudinal second hyperpolarizability per unit length, γ_L^a (a.u.), as a function of the tube radius R.
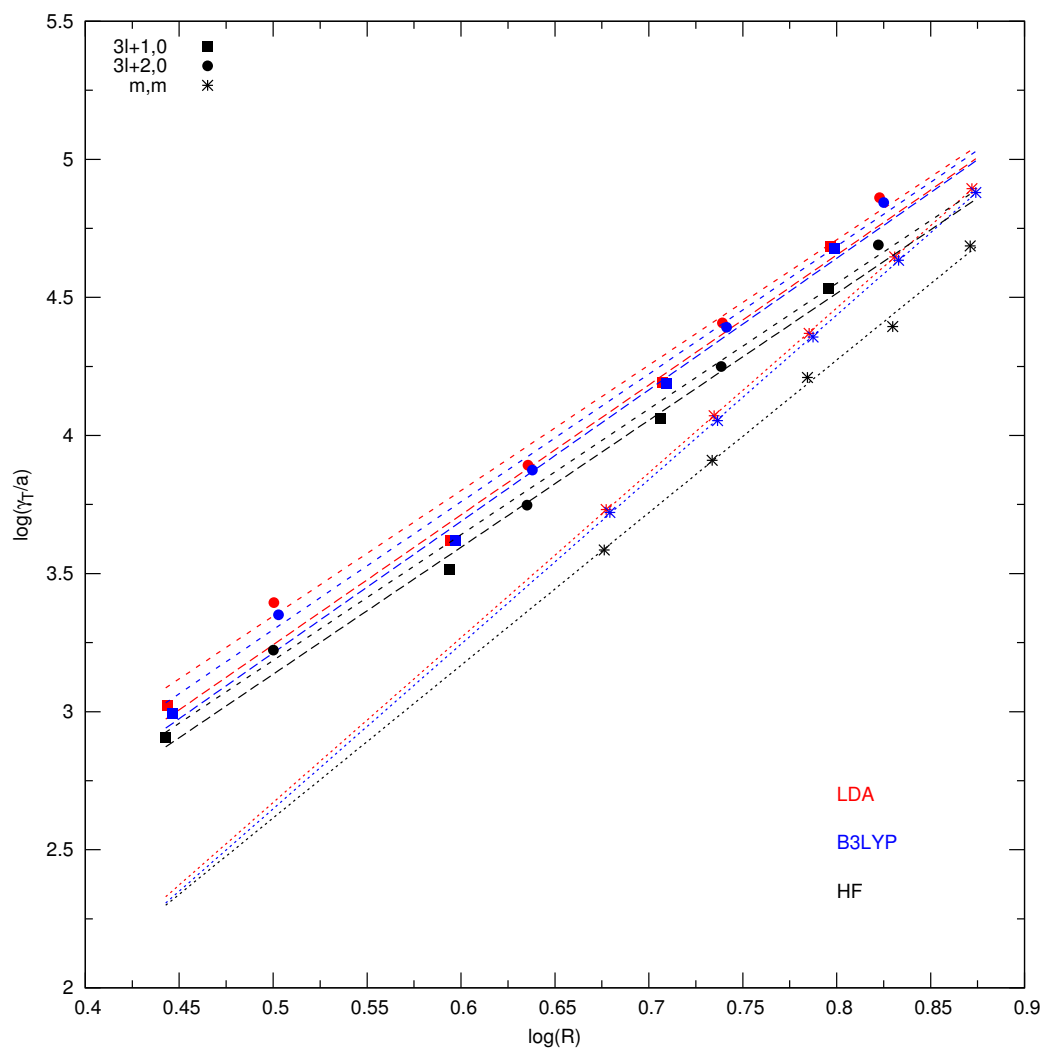
Fig. 6 Logarithmic plot of the transverse second hyperpolarizability per unit length, γ_T^a (a.u.), as a function of the tube radius R.
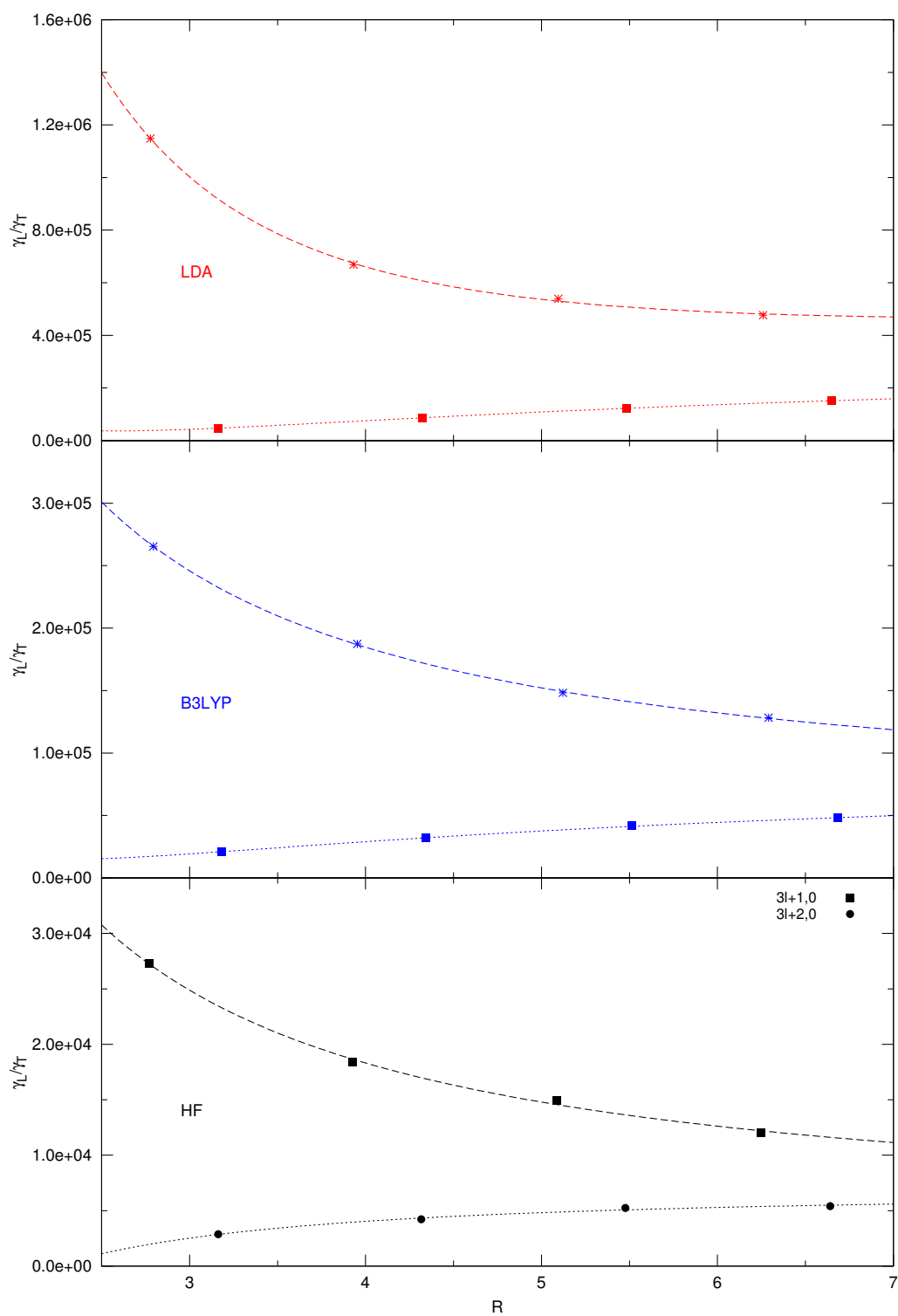
Fig. 7 Ratio between coupled-perturbed longitudinal and transverse second hyperpolarizabilities as a function of the tube radius R (Å).

Table 1 (Hyper)polarizabilities, α^C and γ^C (a.u., values normalized to one C), and energy gap, E_g (eV), of CNTs $(17,0)$ and $(11,11)$ as functions of the shrinking factor S. LDA and HF trends are compared. Note that HF γ_T^C values for the $(11,11)$ tube are affected by some noise. Asymptotic values (by fitting) of γ_L^C are 1.293×10^9 a.u. (LDA) and 2.195×10^7 a.u. (HF); asymptotic values of γ_T^C are 8330 a.u. (LDA) and 4856 a.u. (HF).

		LDA			HF		
	S	α^C	γ^C	E_g	α^C	γ^C	E_g
$(17,0)$	30	152.7	64.0	0.574	74.16	1.600	2.408
	50	151.0	125.2	0.574	74.04	2.187	2.408
$\alpha_L^C, \gamma_L^C \times 10^7$	80	151.0	129.4	0.574	74.03	2.195	2.408
	100	151.0	129.4	0.574	74.03	2.195	2.408
	80	10.53	9194	0.132	9.181	5674	0.500
	100	10.58	6390	0.006	9.252	2915	0.237
	200	10.56	7477	0.006	9.218	4206	0.138
$(11,11)$	400	10.55	7936	0.006	9.207	4726	0.089
	600	10.55	8074	0.006	9.204	4878	0.072
α_T^C, γ_T^C	800	10.55	8140	0.006	9.203	5020	0.059
	1000	10.55	8179	0.006	9.202	5043	0.039
	1500	10.55	8230	0.006	9.206	4813	0.013
	1800	10.55	8246	0.006	9.204	4873	0.017

Table 2 Longitudinal (hyper)polarizabilities, α_L^C and γ_L^C (a.u., normalized to one C), and energy gap, E_g (eV), of CNTs $(17,0)$ and $(11,11)$ as functions of the threshold T_x. Approximate electron-electron interaction maximum distances d_{e-e} (Å) are reported. Results calculated at the HF and B3LYP levels of theory are compared. Asymptotic values (by fitting) of γ_L^C are 3.143×10^7 a.u. (HF) and 4.026×10^8 a.u. (B3LYP); asymptotic values of γ_T^C are 5163 a.u. (HF) and 8064 a.u. (B3LYP).

			HF			B3LYP		
	T_x	d_{e-e}	α^C	γ^C	E_g	α^C	γ^C	E_g
	100	38.25	74.03	2.195	2.408	117.6	34.52	0.920
	200	50.99	74.64	2.567	2.477	118.7	35.60	0.937
	300	63.74	75.00	2.767	2.492	119.2	36.82	0.942
$(17,0)$	400	76.49	75.15	2.883	2.499	119.4	37.64	0.944
	500	84.99	75.23	2.953	2.503	119.5	38.23	0.945
$\alpha_L^C, \gamma_L^C \times 10^7$	600	89.24	75.28	3.004	2.505	119.6	38.63	0.946
	800	106.2	75.31	3.059	2.507	119.7	39.18	0.946
	1000	119.0	75.33	3.087	2.508	119.7	39.36	0.947
	1200	127.5	75.34	3.102	2.509	119.7	39.70	0.947
	1500	144.5	75.35	3.114	2.509	119.8	39.87	0.947
$(11,11)$	100	36.83	9.206	4813	0.013	10.36	7917	0.008
	200	51.56	9.220	4992	0.021	10.36	8024	0.008
α_T^C, γ_T^C	300	63.84	9.224	5066	0.022	10.36	8051	0.008
	350	68.75	9.226	5107	0.023	-	-	-

Table 3 Optimized LDA, B3LYP and HF CNT structures. The coefficients m and n define the chiral vector: $(3l+1,0)$, $(3l+2,0)$ and (m,m) series are separated by horizontal lines. C is the number of C atoms in the unit cell. Cell parameter a and radius R in Å.

			LDA		B3LYP		HF	
m	n	C	a	R	a	R	a	R
7	0	28	4.2438	2.778	4.2625	2.794	4.2349	2.772
10	0	40	4.2458	3.932	4.2651	3.953	4.2372	3.925
13	0	52	4.2459	5.095	4.2656	5.121	4.2374	5.085
16	0	64	4.2458	6.260	4.2656	6.291	4.2375	6.248
8	0	32	4.2407	3.165	4.2583	3.183	4.2265	3.163
11	0	44	4.2433	4.322	4.2620	4.345	4.2313	4.317
14	0	56	4.2441	5.485	4.2634	5.513	4.2338	5.477
17	0	68	4.2445	6.651	4.2641	6.684	4.2349	6.641
7	7	28	2.4504	4.757	2.4629	4.778	2.4466	4.746
8	8	32	2.4506	5.429	2.4631	5.453	2.4469	5.416
9	9	36	2.4508	6.101	2.4632	6.129	2.4471	6.087
10	10	40	2.4509	6.775	2.4632	6.806	2.4472	6.759
11	11	44	2.4509	7.448	2.4632	7.483	2.4472	7.432

Table 4 Longitudinal (L) and transverse (T) polarizability components (in a.u.) normalized to one C. Comparison between coupled-perturbed LDA and HF results. SOS values in parentheses. Energy gap E_g in eV. Horizontal lines separate CNT families according to the chiral vector (m, n): series $(3l + 1, 0)$, $(3l + 2, 0)$ and (m, m).

		LDA			HF		
m	n	α_L^C	α_T^C	E_g	α_L^C	α_T^C	E_g
7	0	120.7(124.3)	5.638(25.92)	0.232	58.12(24.82)	5.339(10.67)	4.335
10	0	119.1(121.0)	6.810(32.68)	0.791	59.79(28.25)	6.304(12.62)	3.546
13	0	135.6(137.1)	8.061(39.65)	0.653	67.18(32.74)	7.324(14.53)	2.940
16	0	155.8(157.1)	9.340(46.62)	0.548	76.03(37.42)	8.353(16.39)	2.508
8	0	91.28(91.78)	6.065(29.46)	0.582	48.19(25.80)	5.650(11.24)	4.604
11	0	107.6(108.3)	7.251(35.75)	0.904	55.95(29.88)	6.631(13.16)	3.672
14	0	128.7(129.5)	8.504(42.51)	0.702	65.40(34.50)	7.653(15.05)	2.970
17	0	151.0(151.9)	9.786(49.39)	0.574	75.34(39.23)	8.682(16.90)	2.509
7	7	-	9.571(36.68)	0.006	-	6.987(13.89)	0.442
8	8	-	6.704(40.30)	0.002	-	7.501(14.68)	0.521
9	9	-	9.091(43.75)	0.005	-	8.070(15.66)	0.568
10	10	-	9.818(47.30)	0.006	-	8.639(16.62)	0.604
11	11	-	10.55(50.90)	0.006	-	9.205(17.56)	0.634

Table 5 Longitudinal second hyperpolarizabilities of semiconductor CNTs normalized to one C, γ_L^C (10^6 a.u.). Comparison between coupled-perturbed LDA, B3LYP and HF results. SOS values in parentheses. CNT series $(3l + 1, 0)$ and $(3l + 2, 0)$ are separated by a horizontal line.

$m, 0$	LDA	B3LYP	HF
7	346.42 (351.57)	75.357 (54.986)	6.3080 (0.9364)
10	557.53 (562.51)	156.68 (96.968)	12.053 (2.3808)
13	1297.1 (1305.9)	354.29 (222.58)	26.593 (6.1150)
16	2891.4 (2905.6)	764.98 (486.15)	51.342 (13.997)
8	29.378 (29.476)	11.856 (7.9576)	1.1983 (0.4496)
11	122.52 (122.25)	43.830 (28.232)	4.2954 (1.4512)
14	451.21 (450.52)	147.76 (93.958)	13.322 (4.3447)
17	1293.9 (1292.8)	397.30 (252.63)	31.212 (10.893)

Table 6 Transverse second hyperpolarizabilities normalized to one C, γ_T^C (10^2 a.u.). Comparison between coupled-perturbed LDA, B3LYP and HF results. SOS values in parentheses. Horizontal lines separate CNT families according to the chiral vector (m, n): series $(3l + 1, 0)$, $(3l + 2, 0)$ and (m, m).

m	n	LDA	B3LYP	HF
7	0	3.0164 (2084.5)	2.8393 (755.13)	2.3133 (79.088)
10	0	8.3345 (6207.8)	8.3637 (2493.5)	6.5422 (259.42)
13	0	24.071 (18555.)	23.907 (7214.3)	17.759 (704.77)
16	0	60.607 (47415.)	59.672 (17714.)	42.799 (1631.4)
8	0	6.2188 (5306.4)	5.6405 (1639.9)	4.1663 (139.81)
11	0	14.219 (11611.)	13.731 (4293.5)	10.170 (399.71)
14	0	36.617 (29759.)	35.441 (10973.)	25.376 (995.88)
17	0	85.612 (69390.)	82.676 (24920.)	57.697 (2173.5)
7	7	19.366 (6086.0)	8.7476 (2831.5)	6.3627 (339.26)
8	8	17.053 (11470.)	16.477 (5079.5)	11.754 (580.76)
9	9	30.118 (20183.)	29.411 (8656.0)	20.855 (940.11)
10	10	51.342 (33956.)	50.132 (14110.)	28.673 (1454.5)
11	11	82.464 (53970.)	80.240 (21860.)	51.069 (2172.5)